

Rethinking Compute Substrates for 3D-Stacked Near-Memory LLM Decoding: Microarchitecture–Scheduling Co-Design

Chenyang Ai*
University of Edinburgh
Edinburgh, United Kingdom
C.Ai-4@sms.ed.ac.uk

Yixing Zhang
Peking University
Beijing, China
2401213080@stu.pku.edu.cn

Haoran Wu
University of Cambridge
Cambridge, United Kingdom
hw691@cam.ac.uk

Yudong Pan
University of Chinese Academy of
Sciences
Beijing, China
panyudong23@mailsucas.ac.cn

Lechuan Zhao
Peking University
Beijing, China
lczhao@stu.pku.edu.cn

Wenhui OU
The Hong Kong University of Science
and Technology
Hong Kong, China
wouab@connect.ust.hk

Abstract

Large language model (LLM) decoding is a major inference bottleneck because its low arithmetic intensity makes performance highly sensitive to memory bandwidth. 3D-stacked near-memory processing (NMP) provides substantially higher local memory bandwidth than conventional off-chip interfaces, making it a promising substrate for decode acceleration. However, our analysis shows that this bandwidth advantage also shifts many decode operators on 3D-stacked NMP back into the compute-bound regime. Under the tight area budget of the logic die, the design of the compute substrate itself therefore becomes a first-order challenge.

Therefore, we rethink the compute microarchitecture of prior 3D-stacked NMP designs. First, we replace prior MAC tree-based compute units with a more area-efficient systolic array, and we further observe that decode operators exhibit substantial shape diversity, making reconfigurability in both systolic array shape and dataflow essential for sustaining high utilization. Building on this insight, we continue to exploit two key opportunities: the high local memory bandwidth reduces the need for large on-chip buffers, and the existing vector core, originally designed to handle auxiliary tensor computations, already provides much of the control logic and multi-ported buffering required for fine-grained flexibility for systolic array, allowing us to unify the two structures in a highly area-efficient manner. Based on these insights, we present the first compute microarchitecture tailored to 3D-stacked NMP LLM decoding, explicitly designed to satisfy the joint requirements of low area cost, high-bandwidth operation, and fine-grained reconfigurability.

To scale the design across multiple cores on one logic die, we further propose an operator-aware scheduling framework that combines spatial and spatio-temporal partitioning for LLM decode operators. Compared with Stratum, our design achieves an average $2.91\times$ speedup and $2.40\times$ higher energy efficiency across both dense and MoE models.

Keywords

3D-Stacked NMP, LLM Decoding, Systolic Array Microarchitecture, Multi-Core Scheduling

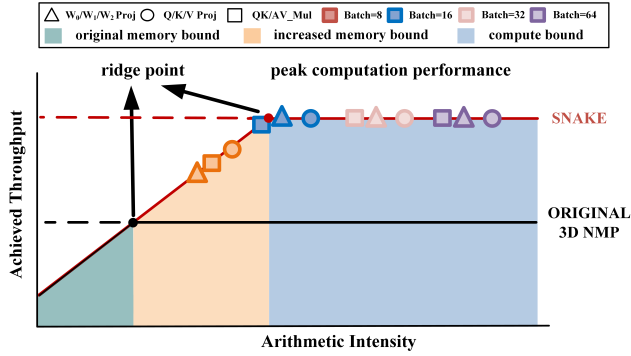
*For any questions regarding this manuscript, please contact me.

1 Introduction

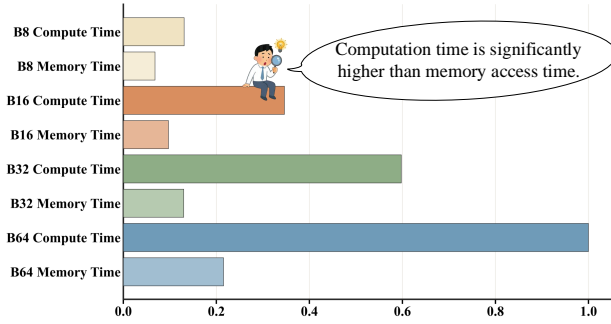
In recent years, Large Language Models (LLMs) have advanced rapidly. LLM inference is typically divided into two phases, namely prefill and decode. Among these, the decode phase is particularly critical, as it directly determines user-perceived responsiveness. Decode proceeds in a token-by-token manner, offering limited weight reuse and leads to low arithmetic intensity. As a result, for both dense and MoE models, end-to-end performance is primarily constrained by off-chip memory bandwidth. Consequently, optimizing LLM decode has become a central focus of recent research [1, 26, 41]

In recent years, 3D-stacked DRAM-based near-memory processing (NMP) has emerged as a promising architectural paradigm for accelerating LLM decode [14, 15, 28, 31, 39]. These designs integrate compute logic directly within the memory stack, typically on a logic-based die beneath multiple stacked DRAM layers. By leveraging dense vertical interconnects, such as Through-Silicon Vias (TSVs) [37] or hybrid bonding [3], NMP architectures enable substantially higher internal memory bandwidth between the logic die and DRAM layers compared to conventional off-chip interfaces. This high-bandwidth, low-latency data access is particularly beneficial for memory-bound operations during decode. Prior work further demonstrates that NMP architectures can operate in a heterogeneous manner alongside traditional xPUs, such as GPUs [5] or TPUs [19], enabling cooperative execution that improves end-to-end LLM inference performance [31, 39].

However, in the 3D NMP setting, many decode tensor operators shift from being memory-bound back to compute-bound. Since decode performance remains primarily dominated by tensor operators, we focus our analysis on matrix multiplication and its associated memory-access behavior from a roofline perspective. As shown in Figure 1a, existing 3D NMP architectures have not scaled on-stack compute capability commensurately with the rapid growth in internal memory bandwidth. Taking Duplex [39] and Stratum [31] as representative 3D-stacked NMP architectures, their compute-to-memory-bandwidth ratio only reaches 8 and 3.7–6.7 FLOPs/Byte, respectively, while decode operators are often required to support batch sizes of up to 64 in practical serving [28, 31], resulting in arithmetic intensity that frequently and significantly exceeds these hardware ridge points. As corroborating evidence in Figure 1b, our reproduction of the Stratum [31] indicates, from the memory-side execution view, that a nontrivial portion of compute



(a) Roofline Analysis of LLM Decode Operators on 3D-Stacked NMP



(b) Memory-Side Execution Analysis of Decode Operators in Stratum. Experiments are conducted using LLaMA3 models across varying batch sizes, and detailed configurations are in Table 1.

Figure 1: Compute-Memory Bottleneck Characterization

latency cannot be fully hidden by double buffering, suggesting that the currently provisioned compute throughput significantly lags behind the available memory supply capability.

Intrinsically, in heterogeneous LLM inference systems, the compute-bound behavior of 3D NMP arises from operator scheduling. Mainstream xPUs typically exhibit ridge points on the order of hundreds of FLOP/Byte or higher [5, 19], making them naturally well suited for high-arithmetic-intensity prefill operators. Although request batching and attention variants (e.g., GQA/MQA) can increase arithmetic intensity, decode operators still remain far below prefill workloads. Therefore, in heterogeneous systems, decode operators are preferentially assigned to 3D-stacked NMP, where even many medium-to-low arithmetic-intensity decode operators become compute-bound thanks to the high local memory bandwidth.

One of the fundamental limitations is the severely constrained area available to the NMP engine on the logic die. At first, the area utilization for compute is limited. Stratum is a representative example: to maintain compatibility with the HBM3 xPU-DRAM interface, the logic die must reserve substantial area for the HBM3 PHY, DRAM peripherals, and power-delivery overhead, which significantly compresses the area budget available for active logic. Then, HBM logic dies remain physically compact—e.g., around 121 mm² in HBM3-class designs—because their footprint is constrained by advanced-package assembly and reliability requirements, a tight

thermal envelope, and poor cost efficiency under die-area scaling [21, 23, 30]. As a result, Stratum reports an active logic area of only about 76.63 mm². In contrast, the neighboring xPU typically exposes only a fraction of the memory bandwidth available on the NMP side, yet can devote an effective compute area that is an order of magnitude larger.

Therefore, this work argues that the compute substrate for 3D NMP should be reconsidered to better match the fundamental characteristics of 3D-stacked systems: lack compute power but severely constrained logic-die area. From the perspective of compute unit, MAC-tree-based designs have been widely adopted in prior work [17, 27, 31, 39] as a mainstream solution. However, as their scale increases, the high-fanout operand buffer delivery paths and multi-stage reduction networks tend to incur substantial interconnect and control overhead, ultimately limiting area efficiency and scalability (detailed in Section 2). In contrast, Systolic Array(SA) organizes a large number of simple processing elements, each performing only basic multiply-accumulate operations, into a two-dimensional structure connected through regular nearest-neighbor links. By exploiting structured data movement, it enables high compute density and array-level data reuse within the fabric, and therefore typically offers superior area efficiency and energy efficiency. This makes it a more suitable compute substrate for area-constrained 3D NMP architectures.

During deployment, we also observed several noteworthy findings. First, Despite these advantages, SA cannot be directly deployed to the LLM decode regime without modification. On the one hand, the operators mapped to a single core during decode exhibit substantial shape diversity, making it difficult for a fixed-shape array to sustain high utilization. This issue is even more important when meeting compute-bound operators. On the other hand, the dimensional relationships among operators also alter the preferable systolic dataflow. This implies that a decode-oriented SA must support reconfigurability in both array shape and dataflow.

On top of the high area efficiency of systolic arrays, we further observe that the 3D NMP setting itself introduces two new optimization opportunities for area efficiency, enabling more compute units to be deployed to alleviate bottlenecks. On the one hand, higher local memory bandwidth weakens the conventional need for large-capacity buffers, making it possible to increase the number of compute units by reducing buffer area. On the other hand, near-memory vector cores already provide fine-grained and flexible control and buffer, which offers a useful foundation for exploring a unified vector-systolic compute substrate, and thus may enable the required reconfigurability at lower area overhead.

Based on these observations, we propose Snake, a reconfigurable SA. Since conventional multi-core scheduling methods fail to adapt to such reconfigurable systolic arrays under high-bandwidth conditions, we also introduce a corresponding multi-core scheduling framework. This work is currently open source at: <https://github.com/aixiii-creator/3d-systolic>. The main contributions of this paper are as follows:

- We observe that current 3D-stacked NMP faces a compute-area bottleneck of LLM decode, motivating the introduction of a reconfigurable SA in both array shape and dataflow. We further identify two architectural opportunities in this

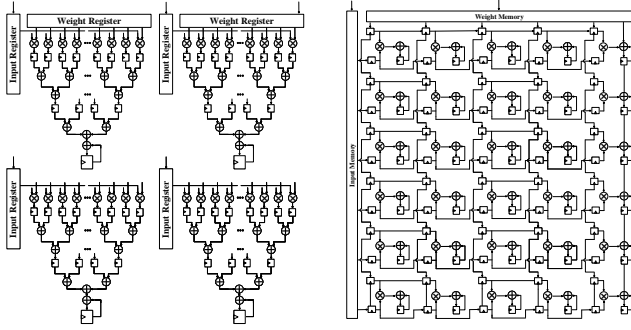


Figure 2: Limitations of SAs for Non-Linear and Reduction Operations

setting that can efficiently realize flexibility while freeing area for additional compute units.

- We propose Snake, a reconfigurable SA whose microarchitecture is optimized for 3D-stacked NMP, meeting the key requirements of LLM decode: high bandwidth utilization, low area overhead, and fine-grained reconfigurability. To achieve this, we introduce a systolic–vector architecture combined with snake-like mapping for area efficiency and high utilization.
- We introduce an multi-core scheduling framework, enabled by a lightweight on-chip interconnect, that fully utilizes the abundant reconfigurable SA and high local bandwidth of 3D-stacked NMP, by revealing the natural alignment between systolic dataflows and spatial/spatio-temporal partitioning.
- Compared with state-of-the-art 3D NMP baseline, Snake achieves $4.00\times$ higher compute-area efficiency, and delivers an average $2.90\times$ speedup and $2.40\times$ higher energy efficiency across diverse LLMs

2 Background

MAC tree and Systolic Array SA and MAC-tree architectures take different approaches to multiply-accumulate (MAC) computation. An SA is a 2D grid of simple processing elements (PEs), each performing only MACs and communicating via nearest-neighbor links. Inputs and weights are fed from array-edge buffers and propagate in a regular pattern, enabling high compute density and efficient data reuse. This simplicity makes SAs area- and energy-efficient for dense, regular matrix workloads.

By contrast, MAC trees place greater emphasis on organizing computation around parallel multipliers and a hierarchical reduction network. As illustrated in the figure 2, a MAC-tree structure feeds a set of parallel multipliers from the weight registers at the top and the input registers on the left, and then progressively reduces the multiplier outputs through a multi-level adder tree to produce the final result. Unlike the regular nearest-neighbor dataflow in SA, this type of architecture incorporates both a high-fanout operand-delivery path and a hierarchical reduction path: the former distributes inputs and weights to multiple multipliers, while the latter incrementally merges multiple product terms across reduction stages. As parallelism increases, the implementation complexity of these two structures in physical layout and timing closure typically

grows further, which can limit area efficiency at large scale. From an energy-efficiency perspective, MAC trees usually require stronger vector broadcast and reduction networks, leading to higher on-chip data-movement energy. Moreover, under batched GEMM workloads, they are less able to exploit array-level data reuse, further degrading energy efficiency. Based on our RTL implementations, the MAC-tree design achieves substantially lower compute density than the systolic-array design, requiring $8.23\times$ more area for the same PE-level compute functionality under the same frequency.

However, SA’s utilization can drop substantially when the workload exhibits the following characteristic. This is a well-known classical challenge, and a large body of prior work has explored this issue [10, 13, 24, 35]. Similar to Snake, prior work has also explored integrating SA with more flexible compute engines, such as CPU [20], GPU [12], or vector-style processing units [29], to better handle irregular workloads and underutilized array regions. However, most existing work is intended to accommodate general matrix multiplications with a wide range of shapes and sizes with more area cost, and their microarchitectures are designed for general-purpose hardware platforms. Snake work identifies area-saving opportunities specific to 3D-stacked architectures and designs a reconfigurable SA with minimal hardware overhead, tailored for LLM decode workloads. In addition, these prior designs mainly focus on single-core usage and ignore inter-layer scheduling.

We further observe that, for LLM decode workloads, enhancing SA utilization yields meaningful speedup only in high-bandwidth 3D-stacked systems. In platforms with lower memory bandwidth, the bottleneck remains memory access, and simply increasing compute throughput provides limited benefit. This indicates that fine-grained systolic arrays optimized for LLM decode are generally effective only in high-bandwidth environments such as 3D-stacked memory systems.

3D-Stacked Accelerators To address the high bandwidth demand of LLM inference, the accelerator have evolved from bank-level in-DRAM processing designs [16, 25, 32] to NMP providing higher compute capability in the logic-layer [39]. Stratum [31] further introduces the co-design of the overall 3D DRAM organization and the hybrid-bonded logic layer. Moreover, some work has also explored scheduling strategies for particular application, such as MoE models [31] and edge deployment [27]. Prior work mainly adopts MAC-tree-based architectures, and the available compute capability remains mismatched with the memory bandwidth.

Although recent works lean toward directly integrating larger compute arrays to study thermal behavior[15] and serving-scale deployment [28], they assume an extremely aggressive large-area logic die, without providing sufficient justification for the manufacturing and packaging feasibility. As a result, many of their conclusions do not hold under realistic HBM3 constraints. SK Hynix [14] attempts to deploy one SA under normal area budget, but they target both prefill and decode simultaneously. This work advocates a heterogeneous architecture that couples conventional XPUs with 3D-stacked NMP, where compute-intensive prefill is handled by resource-rich XPUs, while memory-dominated decode is offloaded to area-constrained NMP logic dies to better exploit their high local bandwidth.

In contrast to prior work, which primarily optimizes 3D-stacked inference from the perspectives of DRAM organization [31, 39], operator mapping [17, 27, 28], and heterogeneous collaboration [39], this work rethinks the compute microarchitecture under the stringent area constraints of the logic die. As such, it is largely orthogonal to existing 3D-stacked memory optimizations and can be combined with them.

3 Key Observations

3.1 Motivation: The Need for Reconfigurability

To provide a unified view of the linear layers in LLMs, we model them as GEMM: the input matrix A multiplies the weight matrix B to produce the output matrix C , where $A \in \mathbb{R}^{M \times K}$, $B \in \mathbb{R}^{K \times N}$, and $C \in \mathbb{R}^{M \times N}$. In a two-dimensional SA, two of the three dimensions, M , N , and K , are typically mapped onto the two spatial dimensions of the array, while the remaining dimension is unfolded temporally. As illustrated in the Figure 3(b), for example, output-stationary (OS) typically maps M and N onto the array’s spatial dimensions and unfolds K over time, whereas input-stationary (IS) typically maps M and K spatially and unfolds N temporally.

In practice, the GEMM dimensions are often much larger than what a single SA can accommodate directly. As a result, the matrices must be partitioned into multiple tiles and executed across multiple rounds. Specifically, when either of the matrix dimensions mapped to the two spatial dimensions exceeds the row or column capacity of the array, spatial tiling becomes necessary. Likewise, if the dimension mapped to the temporal axis is too long, it may also need to be split into multiple sequential phases to avoid on-chip buffer overflow or interruption in data supply. As illustrated in the Figure 3(a), for OS dataflow, when M or N exceeds the array size, tiling must be performed along the corresponding spatial dimension; when K is too large, the computation may further need to be segmented along the temporal dimension. These spatial and temporal tiles naturally form the basic units for later parallel scheduling across multiple cores.

In the LLM decode workloads considered in Figure 3(c), the GEMMs assigned to a single core do not exhibit a fixed shape. During decode, the M dimension is mainly determined by the number of active requests in the batch, and can also vary with the attention configuration, and it still remains much smaller than N and K in most cases. After mapping to a single core, the resulting tiles typically satisfy $N, K \gg M$. Therefore, for the workloads studied in this paper, it is sufficient to consider only OS and IS and exclude WS. This is because a suitable dataflow should place one of the two large dimensions, N or K , on the temporal dimension, so that each tile can run for more cycles once launched. This helps amortize data loading and startup overheads, reduces tile switching, and improves array utilization. By contrast, WS relies more heavily on the much smaller M dimension and is therefore less suitable for this decode setting.

Firstly, this workload characteristic motivates array-shape reconfigurability. Conventional SAs typically use a fixed shape, often a near-square one, to achieve balanced utilization for general GEMM workloads. In LLM decode, however, the M dimension is often smaller than the array dimension mapped to it, causing many PEs to remain idle. Although utilization may improve at larger

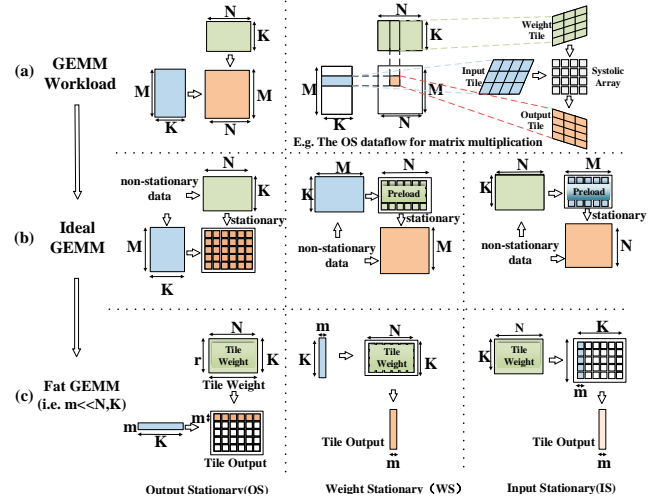


Figure 3: GEMM Abstraction and Systolic Dataflows

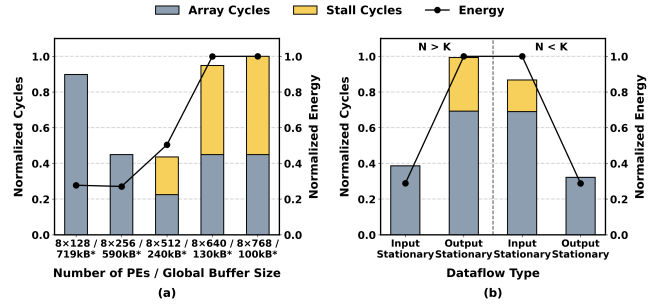


Figure 4: Impact of Buffer Allocation and Dataflow Choice on Decode Execution

batch sizes, it can still vary substantially across layers and requests. As discussed earlier, the abundant local memory bandwidth in 3D-stacked NMP often shifts decode execution into the compute-bound regime. As a result, utilization loss no longer only wastes hardware resources, but can directly translate into higher latency. Such mismatch also weakens buffer data reuse and reduces energy efficiency, which will be verified later.

Also, this workload characteristic motivates reconfigurability of systolic dataflow. More specifically, when $N > K$, IS is generally preferable because making N the temporal dimension reduces the repeated re-tiling and rereading overhead along the N dimension. Conversely, when $K \geq N$, OS is more favorable because it unfolds K temporally. As also illustrated in the Figure 4(b), even frequently occurring tiled workloads may exhibit different preferred mappings at different times.

3.2 Opportunity 1: High Local Bandwidth Enables Buffer-to-Compute Reallocation.

In conventional SA constrained by off-chip bandwidth, on-chip SRAM buffers are typically large for two reasons. First, they support double buffering, so that one region supplies the current tile while another prefetches the next tile to hide memory latency. Second, they keep inputs, weights, and partial sums on chip for reuse. As a result, buffering occupies a large fraction of area. By contrast, each

PE implements only simple MAC logic and is much smaller than large SRAM arrays.

Under NMP, the high local bandwidth of 3D-stacked memory and the lower cost of data movement weaken these conventional reasons for large buffers. Meanwhile, as discussed earlier, decode becomes more likely to be limited by effective compute supply. To examine this opportunity, we use OPT 66B at batch size 8 as a representative decode workload. We allocate most of the SRAM budget to the weight buffer and keep the input and output buffers small. We then keep the total area budget fixed, gradually reduce SRAM capacity, and use the reclaimed area to increase the number of PEs, thereby exploring a buffer–compute reallocation space.

Figure 4(a) shows the trade-off. As the PE count increases from 8×128 to 8×512 , array cycles drop significantly, showing that the benefit of extra compute outweighs the loss of buffer capacity. However, when the configuration is further scaled to 8×640 and 8×768 , stall cycles and energy rise sharply, indicating that the buffer has become too small to sustain efficient data supply, and the array dimensions also introduce unfavorable tile mismatch. We therefore choose an elongated 8×512 physical organization as the PE configuration. As shown later in Section 6.6, batch size 8 corresponds to the highest weight-buffer demand; at higher batch sizes, allocating more area to computation brings even larger performance and energy benefits.

This result highlights two effects. First, for compute-bound decode operators, more compute units relieve the bottleneck more effectively, and the larger array can also reduce tile folds, lowering both compute and memory latency. Second, under high-bandwidth NMP, data staging and prefetching complete much faster, so large double-buffered SRAMs are less necessary. Even when a smaller buffer occasionally causes extra DRAM accesses, the penalty is much lower than in conventional off-chip-bandwidth-limited platforms. Prior work reported a similar trend. TETRIS [8] targets CNN/FC inference and uses an Eyeriss-based [4] accelerator in each 3D-memory vault to shift area from the global buffer to more PEs. Our work instead targets shape-diverse LLM decode and uses the reclaimed area not just for more fixed compute, but for a reconfigurable systolic substrate that adapts both array shape and dataflow to the workload.

3.3 Opportunity 2: Unifying Vector-Style Flexibility with Systolic Efficiency.

Existing 3D NMP designs follow different architectural paths [15, 28, 31], but they ultimately require two classes of capability at the same time. The first is high-density computation for tensor MAC operations. The second is flexible execution support for nonlinear operators, reductions, element-wise processing, and fine-grained control. The former aligns naturally with systolic execution, whereas the latter is more closely associated with vector-style execution.

In 3D-stacked NMP, the area budget on the logic die is extremely constrained. Our earlier analysis shows that decode workloads require not only high-density MAC capability, but also flexibility to accommodate dynamic variation in array shape and dataflow. This suggests that a more promising direction is not to mechanically place a vector core beside a SA, but rather to build a unified compute substrate that reuses vector-side control, buffering, and reduction

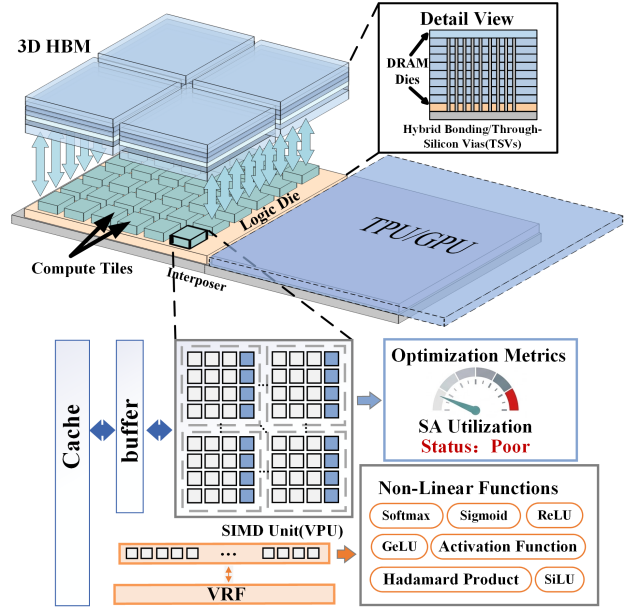


Figure 5: Overview of a 3D-stacked NMP system architecture.

support to provide vector-style flexibility together with systolic-style efficiency.

4 Architecture

4.1 Overview

Prior 3D NMP systems largely share a common stack-level template: logic-die-side compute engines are tightly coupled with stacked high-bandwidth memory. This work targets a different layer of that design stack. Rather than redesigning the memory stack itself, we focus on the compute substrate on the logic die and develop an architecture that can be instantiated under similar stack-level assumptions, and the detailed reference setting is described in Section 6.1.2. The external xPU remains responsible for host-side coordination and complementary execution of operators from LLM prefill. In evaluation, we instantiate this organization using an HBM3 configuration consistent with prior 3D NMP studies.

At the logic-die level, we organize the stack into 16 processing units (PUs) connected by a lightweight NoC, which is used only for coarse-grained communication such as all-reduce and all-gather. Each PU is bound to one memory channel and forms a locality-preserving compute-memory tile. Inside each PU, four compute cores are integrated, each built around a 64×64 PE array and equipped with its own private systolic buffer, while vector-style processing support is provided at the PU level. This organization matches the naturally distributed, NUMA-like structure of 3D NMP, where local channel access is preferred and fine-grained remote accesses are minimized. Within a PU, the four compute cores cooperatively execute the assigned local workload. To efficiently feed these cores, banks in the local channel are grouped into bank bundles for parallel tile refill. Data fetched from these bank bundles

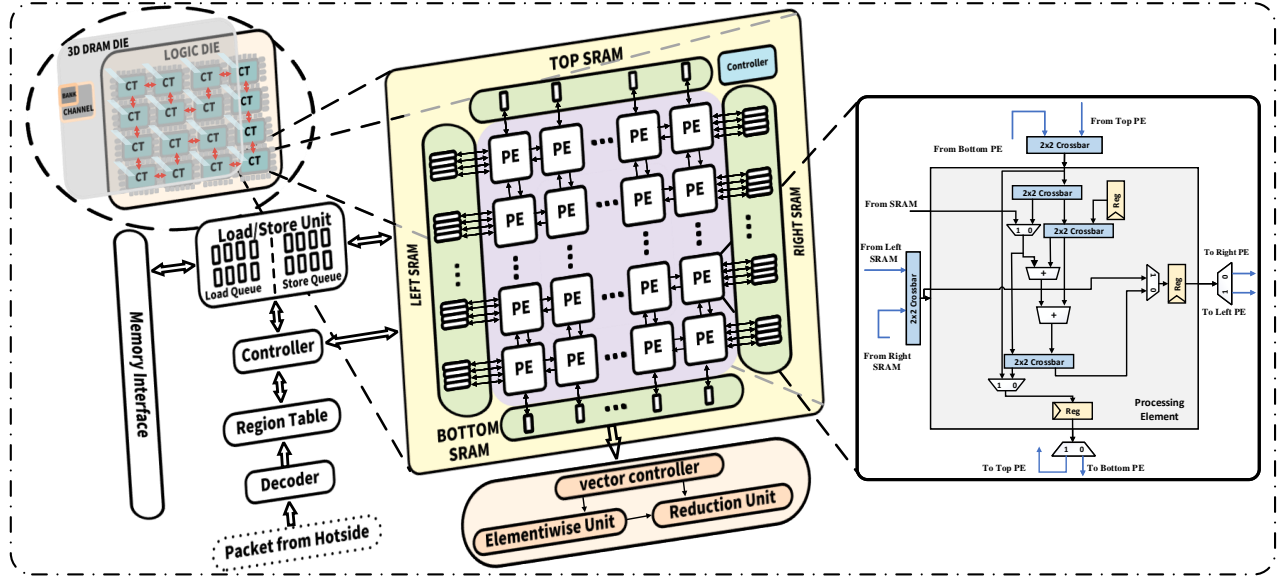


Figure 6: Architecture Overview.

are first staged in the private systolic buffers, which provide light-weight layout reorganization and double-buffered tile supply before delivering tile-ready operand streams into the local systolic arrays.

4.2 Core Microarchitecture

Following the analysis in Section 3.3, we tightly integrate the vector core with the systolic array, so that the fine-grained execution substrate of the former can be reused to support fine-grained computation and reconfiguration in the latter.

4.2.1 Array Design. As discussed above, our design already exploits the high local memory bandwidth of 3D-stacked NMP to reduce on-chip buffering and reallocate more area to PE arrays, thereby increasing compute density under the tight logic-die area budget. However, even after reducing the overall buffer footprint, the cost of reconfigurability itself remains a major concern. In a fine-grained reconfigurable systolic array, multi-ported buffers are still required to support sub-array reshaping and dataflow switching under different logical mappings, and prior work has shown that they are among the dominant area costs of such designs [13]. Therefore, the key objective of our array design is not only to shrink total buffer capacity, but also to further minimize the multi-port overhead needed for reconfiguration.

To make room for this capability, we reclaim part of the vector-side multi-ported buffering budget. In conventional *Tensor Core + Vector Core* LLM accelerators [15, 31, 38], the vector core typically relies on a heavily provisioned multi-ported local buffer to sustain reductions such as sum/max and element-wise post-processing at high standalone throughput. In our design, we do not preserve such a private buffer. Instead, we redirect part of that area to the SA side, where multi-port support more directly improves the utilization of

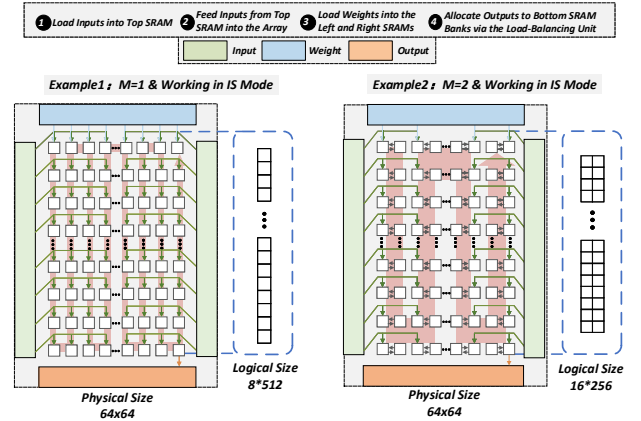


Figure 7: Serpentine Logical Array Remapping under IS Dataflow.

small- M decode operators mapped onto a large physical array. This trade-off is reasonable because vector-side nonlinear and reduction operators in LLM inference are typically small in scale and highly pipeline-friendly, so their latency can often be overlapped with preceding or subsequent GEMM execution [31]. As described later, we further tighten this integration by allowing the SA and the vector core to share a common 2-read/2-write output buffer, similar to Gemmini [9], instead of maintaining separate multi-ported storage structures as in prior 3D-stacked NMP designs [31, 39].

Unlike conventional SA, our design surrounds the PE fabric with four boundary buffers on the top, bottom, left, and right sides. This organization provides the structural basis for flexible remapping under different logical array shapes and dataflows. However, not all

four sides require the same degree of flexibility: since fine-grained remapping is only needed along the small- M dimension, multi-port support is required only for weight injection. Specifically, if the array is partitioned into g logical slices, then g weight-injection ports are needed in total. As shown in Figure 6, the central yellow region in the figure corresponds to a single PE array at the core level. We adopt a symmetric left-right boundary organization for the weight side, so that these ports can be distributed across the two boundaries rather than concentrated on one side. For example, when the remapping granularity is 8, only four ports need to be activated on the left boundary and four on the right boundary. This significantly reduces the per-side multi-port requirement of the weight buffer and boundary interconnect under the tight logic-die area budget of 3D-stacked NMP. Inside each PE, configurable crossbars and register paths support directional data propagation, enabling the logical communication pattern to be reorganized under different sub-array shapes and dataflows. In addition, As shown in Figure 6, the rightmost zoom-in shows the microarchitecture of an individual PE. The bottom-boundary PEs introduce extra interconnect paths to support different output-propagation patterns. The mapping is constrained to a serpentine traversal so that reshaping only requires local PE-to-PE redirection, rather than expensive global interconnect or arbitrary cross-array routing [13, 35]. This not only lowers the reconfiguration cost, but also improves scalability, since the wiring and control remain local as the array grows.

On top of this low-cost multi-port organization, we propose a fine-grained systolic-array mapping method, termed *snake-like mapping*, in which the dataflow propagates through the physical PE fabric along a serpentine path, much like the Snake game gradually sweeping across and filling the entire array. Figure 7 illustrates this remapping under the IS dataflow. A physical 64×64 array serves as the fixed PE fabric. In this example, inputs are loaded into the top buffer, weights stream into the array from the left and right buffer, and the output space is distributed across different bottom SRAM banks by the SRAM load-balancing unit. Under this organization, the same physical 64×64 array can be remapped into different elongated logical sub-array shapes to better match operators with different small- M dimensions. When $M = 8$, the entire physical array is reorganized into a logical 8×512 sub-array. In other words, the original two-dimensional set of 4096 PEs is traversed in a snake-like manner and concatenated into a longer logical computation path, allowing each logical output stream to propagate through the full PE fabric and accumulate continuously. Likewise, when $M = 16$, the same physical array is reorganized into a logical 16×256 structure, enabling more parallel logical output streams while preserving a long effective computation path. Although our minimum reconfiguration granularity is 8 rather than 1, this limitation mainly affects a small subset of GEMV-like decode operators with extremely small M (e.g., $M = 1$), which cannot be perfectly matched by our logical sub-array shapes. This design choice is acceptable because such cases tend to become memory-bound, where execution is dominated by data-supply stalls rather than peak compute occupancy. In such cases, the residual utilization loss has limited impact on end-to-end performance.

4.2.2 Vector Core Design. The vector core is organized around the shared output buffer of the systolic array, rather than using

a separate private SRAM. In this way, the same storage structure serves both as the writeback space for SA results and as the input/intermediate buffer for subsequent vector operations such as softmax, normalization, and other element-wise processing. To support this interaction, the shared buffer is implemented as a banked 2-read/2-write structure. The systolic array can write results back to the buffer, while the vector core reads them out for post-processing. A lightweight arbitration logic coordinates array writeback, array readback, and vector-side accesses according to access type and bank conflicts. This organization preserves limited overlap between tensor and vector execution when accesses do not conflict, while keeping the vector-side storage overhead small under the tight logic-die area budget.

4.2.3 Control Logic Design. The controller originally used on the vector side for fine-grained operator scheduling is extended to manage sub-array activation/deactivation, region allocation, dataflow configuration, and readiness tracking, thereby elevating what was originally a vector-only fine-grained control plane into a lightweight shared scheduling substrate for both the Tensor Core and the Vector Core. Following prior vector processor inspired control organizations, so we employ the following control modules.

Decoder. The Decoder receives task packets from the host side and parses them into internal execution descriptors.

Load/Store Unit (LSU). The LSU manages on-chip SRAM at bank granularity, including operating-mode selection, address allocation, and dataflow-direction control. It also contains internal load/store queues to coordinate input prefetching, weight loading, and distributed output writeback, thereby supporting dataflow switching across different logical shapes while hiding storage-access latency as much as possible.

Region Table (RTAB). The RTAB records the spatial boundaries of each working region together with its corresponding SRAM allocation results. During execution, it continuously tracks the readiness, running, and completion states of all regions, enabling dynamic management of multiple logical sub-arrays.

5 Multi-Core Scheduling via Spatial and Spatio-temporal Partitioning

We realize this multi-core scheduling at the PU granularity, where each PU comprises four local cores that share the assigned computation. We develop a PU-level scheduling method for reconfigurable fine-grained SA cores, targeting the shape characteristics of LLM decode operators. Within each PU, its four local cores cooperatively share the assigned computation and use the same systolic dataflow configuration for a given operator.

a) Intra-operator multi-PU scheduling.

In this part, we only consider how multiple compute PU cooperate to execute one linear operator. As discussed in Section 3.1, the preferred single-core systolic dataflow depends on the relative size of N and K . Multi-PU scheduling preserves the same OS/IS dataflow choices as in the single-core case, but the final scheduling mode is jointly determined by the original task shape and the spatial/temporal partitioning across PU.

We therefore turn to the view of MNK-level partitioning. First, we do not partition the M dimension across PU like other works did [31, 39], because this would replicate large weight matrices

across multiple PU and significantly increase on-chip communication and storage pressure. Therefore, we keep the M dimension inside each PU and only design multi-PU scheduling over the two dominant dimensions, N and K . Under IS and OS, these two dimensions naturally serve as the spatial and temporal dimensions in different ways. As a result, the multi-PU design space reduces to four partitioning modes.

1) IS-S: IS with pure spatial partitioning. In this mode, IS is used as the inter-PU dataflow, and only spatial partitioning is applied across PU. Different PU mainly split the K dimension in space, while each PU locally processes its tiles along the N time dimension.

2) IS-ST: IS with spatio-temporal partitioning. This mode extends IS-S by further partitioning the time dimension. Besides splitting the K dimension in space, it also divides the time dimension N into multiple stages or time blocks.

3) OS-S and 4) OS-ST. Similarly, OS-S partitions the N dimension in space and advances along the K dimension in time. OS-ST further partitions the K dimension into multiple time blocks based on OS-S.

This lightweight interconnect design is also driven by the above tiling characteristics, which keeps the communication structure simple and area-efficient. As shown in Figure 8, the same 16 PU can be organized in two simple logical ways using interconnect: a snake-like 1×16 chain, similar to the traversal described above, or a regular 4×4 mesh, similar to a conventional array interconnect. The 1×16 view is used when one dimension is divided by 16 across the 16 cores, corresponding to *IS-S* and *OS-S*. The 4×4 view is used when both dimensions are divided by 4 across PU, corresponding to *IS-ST* and *OS-ST*.

b) Operator-specific scheduling analysis. These four modes define the MNK-level scheduling space for the major linear kernels in decode. The proposed framework can be applied to various operator-level scheduling strategies [17, 28, 31]; below, we provide one illustrative example. We first decide which operators are scheduled within this space and which are better handled separately. We also analyze tile-level overlap between these linear operators and the following nonlinear stages to reduce end-to-end latency.

For the QK and AV head-level operators in attention, the computation of one head is usually small and short, and thus cannot fully hide the memory access latency from 3D-stacked memory. Therefore, we follow a strategy similar to Stratum [31]: we mainly use head-level parallelism, map different heads to different PU, and improve utilization by interleaving the linear stage and the Softmax/reduction stage of different heads within the same group.

For the remaining decode operators that account for most of the execution time, such as projection layers and expert FFNs in MoE layers, we treat them as independent GEMM/GEMV kernels and analyze their dataflow choices under the above multi-PU spatial/spatio-temporal framework.

In general, OS dataflow is more favorable for direct tile-level overlap between linear and nonlinear stages, because an output tile can be consumed by the following nonlinear operator as soon as its in-array reduction is completed. By contrast, under IS dataflow, such direct overlap is usually weaker, since an output tile often becomes available only after accumulation along the temporal dimension is finished. Fig. 9 shows one representative example of this

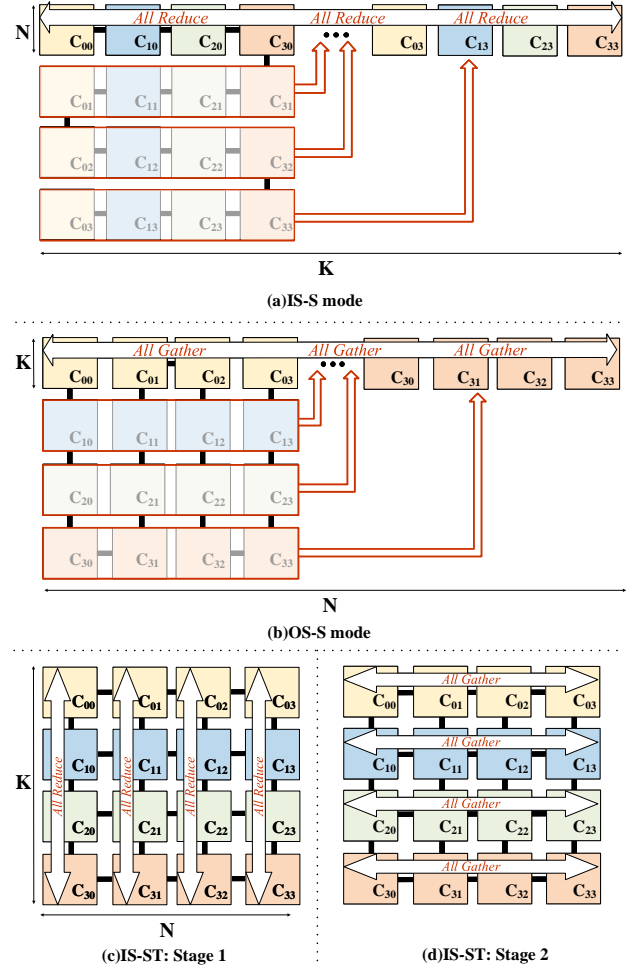


Figure 8: Logical Inter-PU Organizations for the Four Partitioning Modes

difference. Still, IS can remain favorable when it shortens the critical GEMM latency, and it may also exploit overlap across independent operator branches. In practice, the realizable overlap further depends on whether the following stage is tile-foldable, as well as on the communication pattern (e.g., all-gather vs. all-reduce), buffer-capacity constraints, and broader DAG dependencies. For a given LLM, our simulator can quickly evaluate this compact and practical search space. It analyzes the network structure layer by layer and applies the corresponding scheduling search to each operator.

6 EVALUATION

6.1 Experimental Setup

6.1.1 Benchmark. We follow Helios [28] in benchmark selection and use OPT [40], LLaMA3 [11], Mixtral [18], Qwen3 [33], and DeepSeek [7]. These models cover both dense and MoE LLMs. We use model-specific input/output length settings for decode and serving evaluation. Detailed configurations are summarized in Table 1.

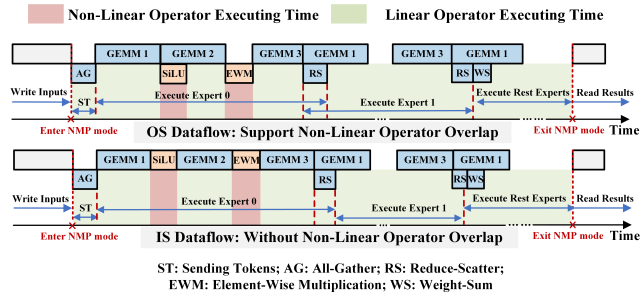


Figure 9: A Representative MoE-Expert Example of Linear-Nonlinear Overlap under OS and IS Dataflows.
Table 1: Architectural configurations of evaluated models.

Model	L	(H, F)	(Q, KV)	Configuration
OPT 66B	64	(9216, 36864)	(72, 72)	Dense, MHA
LLaMA3 70B	80	(8192, 28672)	(64, 8)	Dense, GQA
Mixtral 8×22B	56	(6144, 16384)	(48, 8)	MoE, E=8, top-2
Qwen3 30B-A3B	48	(2048, 768)	(32, 4)	MoE, E=128, top-8
DeepSeek 236B	60	(5120, 1536)	(128, 128)	MoE, E=160, top-8, MLA

6.1.2 Baseline. Our goal is to compare compute microarchitectures under a realistic 3D-stacked memory-system setting, rather than target any single prior design. We therefore use a common hardware configuration as the deployment reference and evaluate all compute substrates under this unified setting.

Although Stratum [31] is primarily designed for MoE serving, it provides a suitable and well-documented 3D-stacked NMP template for general LLM inference. We therefore adopt Stratum’s hardware configuration, including its memory-system assumptions such as DRAM organization, timing, and energy parameters, but fix the effective DRAM bandwidth at 24 TB/s in our evaluation to reflect the overall power-budget constraint. Since our architecture adopts a compute hierarchy structurally similar to Stratum, we use the same number of PUs under the same logic-die area budget for a direct area-normalized comparison. We further introduce two fixed-shape systolic-array baselines: a square 48×48 array and a long 8×288 array. Under the same 3D-NMP logic-die constraints, these designs represent practical fixed-shape alternatives without the microarchitectural flexibility enabled by our reconfigurable architecture. We keep all other system-level assumptions unchanged. The fixed-shape baselines are assumed to operate at up to 1 GHz, whereas our design targets 800 MHz due to the additional routing constraints introduced by reconfigurability; thus, our comparison is area-normalized but implementation-aware rather than iso-frequency.

6.1.3 Modeling. Using SystemVerilog, We implement our architecture by modifying PLENA [38], a representative LLM SA design, and adapt its original flattened systolic substrate into a reconfigurable SA for the 3D-stacked near-memory setting configured in IEEE754 FP16 under the 7 nm ASAP7 predictive PDK [6]. The local buffer on the logic die are implemented as SRAM macros, modeled using FinCACTI [36] and calibrated with publicly available SRAM specifications [2]. Dynamic energy is estimated from the

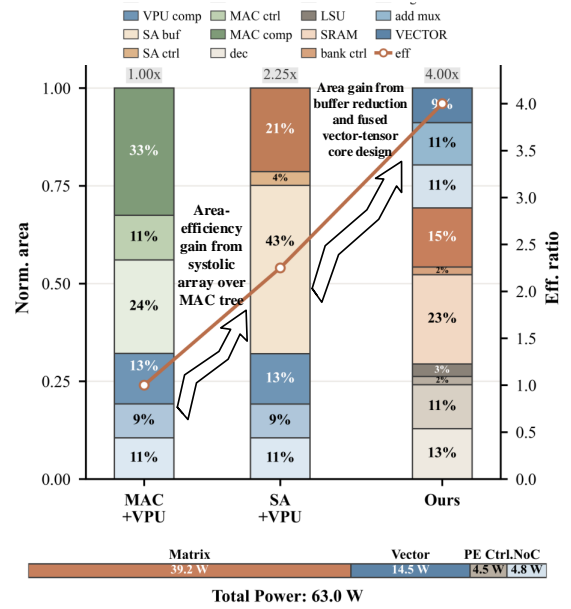


Figure 10: Normalized area breakdown and compute-area efficiency

post-synthesis gate-level netlist with switching activity annotated from simulation.

For kernel-level performance modeling, we build on Scale-Sim v3 [34], which integrates the Ramulator [22] memory model, and extend it to capture systolic-array execution in a 3D-NMP setting, including multi-PU interconnection and vector-core support. Directly invoking SCALE-Sim during serving-time replay is prohibitively expensive, because repeated decode-time queries incur substantial runtime overhead from retained per-layer simulator state and explicit SRAM trace generation. We therefore adopt a lookup-based flow that reuses previously simulated decode points indexed by workload shape and hardware configuration, and execute cache misses in adaptively reduced chunks to bound peak memory usage.

For end-to-end serving evaluation, as well as GPU and MAC-tree baseline characterization, we build on Duplex’s system-level serving framework [39], including Poisson-based request injection under varying arrival rates, continuous batching, and latency accounting. We use NVIDIA H100 as the common prefill engine across all compared systems, and also use H100-only decoding as one baseline. Within the Duplex-based simulator, we retain its internal GPU and NVLink models and incorporate a Stratum-configured MAC-tree backend for comparison. We evaluate all models on an 8-device system with tensor parallelism degree $TP=8$. Although our reconfigurable SA can potentially support more flexible scheduling for MoE expert layers in 3D NMP [17], we intentionally retain TP for these layers in this work to avoid conflating backend improvements with a different MoE partitioning policy and to maintain balanced workload distribution, as in [31, 39].

6.2 Area Analyze

Figure 10 compares the normalized area breakdown and compute-area efficiency of three designs at single-PU granularity. All three

designs are compared under the same PU-level area budget of 2.35 mm^2 .

Replacing the MAC-tree engine with SA already brings a clear improvement: SA + Vector Core reaches $2.25\times$ higher compute-area efficiency. This gain mainly comes from the structure of the SA with higher compute density. Our design further improves area efficiency in two ways mentioned before, and achieves $4.00\times$ compute-area efficiency over the MAC Tree. From the area breakdown, the total buffering-related area decreases from 53.6% in SA + VECTOR CORE to 22.8% in OUR WORK, releasing 30.8% points of PU area, and this released area is mainly reallocated to the compute units. The vector-core share also decreases to 8.8%, and part of it is further reallocated to the fine-grained control logic and compute units.

Figure X shows the power breakdown at peak performance. The total logic-die power is 63.0 W, including 39.22 W for Matrix, 14.47 W for Vector, 4.47 W for PE control, and 4.84 W for NoC. Although the SA-based design has somewhat higher peak power than MAC-tree, it can be further adapted to a 3D NMP thermal budget by moderately reducing the DRAM bandwidth. Meanwhile, it can be further adapted to a 3D NMP thermal budget by moderately reducing the DRAM bandwidth operating point. Meanwhile, our design also achieves higher energy efficiency by reducing unnecessary on-chip SRAM accesses and shortening overall runtime.

6.3 Decode Performance Evaluation

Prior work [15] has established that thermal dissipation at the logic die is the primary bottleneck in 3D-stacked systems. Therefore, this work focuses specifically on comparing the energy consumption of the logic die. As shown in Fig. 12, compared with GPU, our design achieves an average of $11.47\times$ speedup and $5.74\times$ higher energy efficiency. Compared with the MAC-tree baseline, our design achieves an average of $2.90\times$ speedup and $2.40\times$ higher energy efficiency. These gains come from both a denser compute organization under the tight logic-die area budget and better workload matching through reconfigurable dataflow and Multi-PU scheduling. Meanwhile, by reducing unnecessary on-chip SRAM accesses and shortening execution time, our design also improves energy efficiency.

Further comparison with the two fixed-shape systolic-array baselines shows that reconfigurability itself is a key source of the gain. Compared with the 48×48 SA baseline, our design achieves an average of $2.33\times$ speedup and $1.05\times$ higher energy efficiency; compared with the 8×288 SA baseline, it achieves $3.00\times$ speedup and $1.31\times$ higher energy efficiency on average. Although a fixed-shape systolic array may achieve better local reuse for some operators, the reconfigurable SA can select a more suitable array shape for each operator, thereby improving both throughput and memory-access energy efficiency.

6.4 Serving Performance Evaluation

Fig. 11 presents the latency results of five models under two serving scenarios: the top row reports end-to-end (E2E) latency under full serving, while the bottom row reports time-between-token (TBT) latency under decoding stress tests.

Fig. 11 shows normalized serving latency under different request rates for 8K-input and 1K-output requests. The x-axis is the normalized request rate, and the y-axis reports normalized latency, including both end-to-end (E2E) latency and time-between-tokens (TBT) latency, with our design as the baseline.

Specifically, the GPU baseline exhibits substantially higher latency. As shown in the figure, GPU E2E latency is typically around $1.5\times\text{--}3.0\times$ that of our design, while its TBT latency usually reaches about $1.5\times\text{--}4.0\times$. MAC-tree is generally the closest baseline to our design, with E2E latency mostly around $1.1\times\text{--}2.3\times$ that of our design and TBT latency mostly around $1.3\times\text{--}2.2\times$. As the request rate increases and the effective decode batch becomes larger, the area-efficiency advantage of systolic arrays becomes more consistent. Since our design can further adapt both array shape and mapping strategy to the workload, it gradually widens the gap over MAC-tree.

For fixed-shape systolic arrays, the 48×48 SA consistently performs better than the 8×288 SA, but both remain inferior to our design. In particular, the 48×48 SA still shows about $1.1\times\text{--}2.4\times$ E2E latency and $1.1\times\text{--}2.2\times$ TBT latency of our design, while the 8×288 SA is often worse, with TBT latency reaching about $1.5\times\text{--}4.5\times$. This suggests that a near-square array is more robust than a highly elongated one under serving workloads. Still, both fixed-shape designs suffer from workload-shape sensitivity, whereas our reconfigurable array can sustain higher utilization across more diverse decode workloads.

6.5 Multi-PU Scheduling Analysis

Figure 13(a) shows the per-layer selection of systolic dataflow strategies under varying batch sizes and input sequence lengths. We include one dense model (LLaMA3 70B) and one MoE model (Qwen3 30B-A3B) for comparison. For the dense model, strategy selection is highly concentrated, with IS-S dominating (59.7%), followed by OS-S (25.0%), IS-ST (12.5%), and OS-ST (2.8%). In contrast, the MoE model exhibits a more balanced distribution across IS-ST (33.3%), IS-S (27.8%), OS-S (20.8%), and OS-ST (18.1%). This illustrates that optimal dataflow and partitioning strategies vary significantly across layers, making it challenging for any single fixed strategy to achieve consistently high utilization.

Figure 13(b) compares decode latency when all layers are constrained to a single fixed strategy versus using our per-layer flexible scheduler. For LLaMA3 70B, the best fixed strategy (OS-ST) still incurs a slowdown of $1.04\times\text{--}1.56\times$ relative to the per-layer scheduler. The impact is more pronounced for Qwen3 30B-A3B, where the best fixed policy experiences a slowdown of $1.18\times\text{--}6.43\times$. These results highlight that a per-layer, workload-adaptive strategy is essential to approach optimal decode performance across diverse layers and sequence lengths.

6.6 Array-Shape and Buffer Trade-offs

Figure 14 illustrates the difference in array-shape demand between two representative large models during decoding under a fixed PE budget of 4096. The top panel shows the contribution of different array shapes to the total oracle cycles across all configurations in Section 6.3. For the dense model LLaMA3 70B, the demand is mainly concentrated on near-square arrays, whereas the MoE model

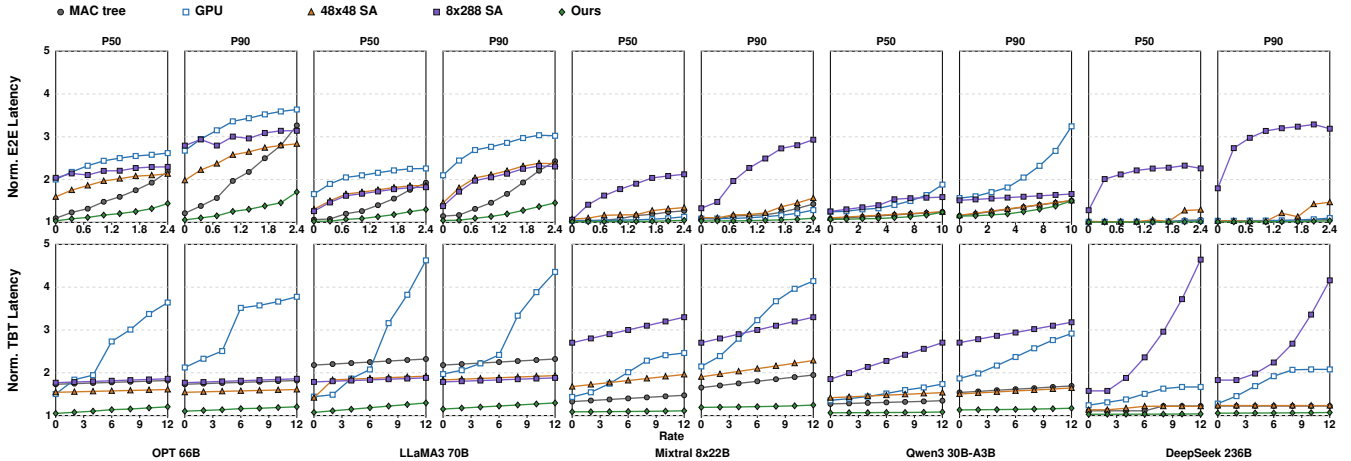


Figure 11: Normalized Serving Latency Under Different Request Rates

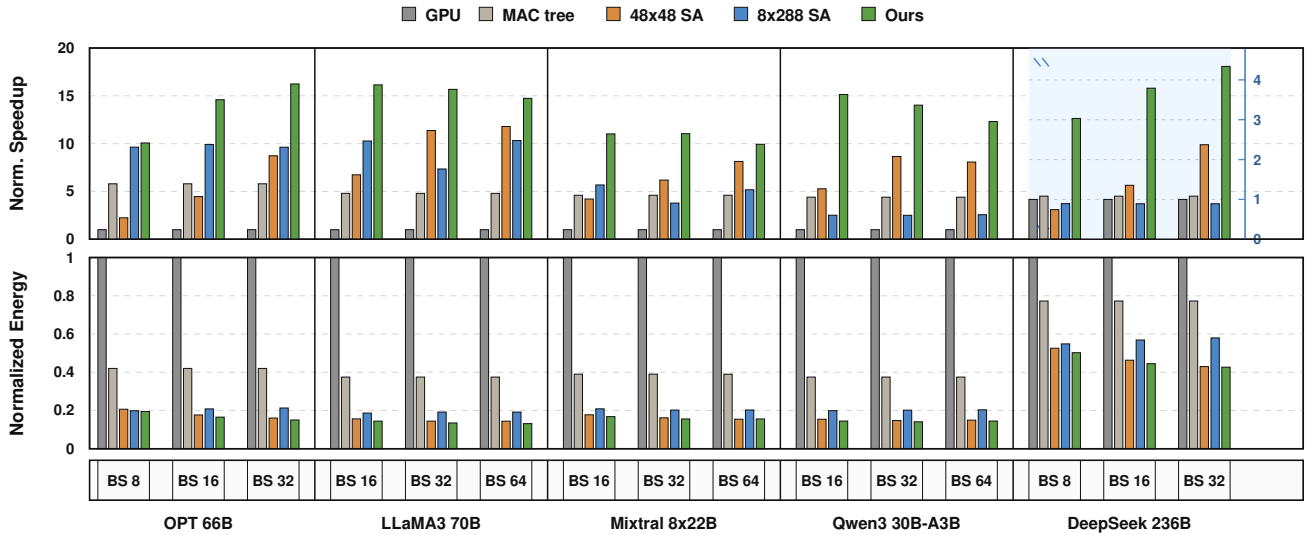


Figure 12: Normalized Decode Performance and Energy Efficiency

Qwen3 30B-A3B shows a clear preference for rectangular arrays. As the array evolves from a highly elongated 8×512 shape to a more square 64×64 shape, the filter-buffer requirement drops significantly: for LLaMA3 70B, it decreases from 256 KB to 64 KB, and for Qwen3 30B-A3B, it decreases from 64 KB to 16 KB. In contrast, the activation-side buffer requirement increases steadily, from 16 KB to 72 KB for LLaMA3 70B and from 8 KB to 24 KB for Qwen3 30B-A3B. This trend reveals a clear trade-off between the two types of buffering, which provides useful guidance for design-space exploration.

7 Conclusion

By co-designing a reconfigurable systolic array with multi-core, multi-core scheduling, SNAKE efficiently leverages the high local bandwidth of 3D-stacked NMP to deliver substantially improved

LLM decode performance and energy efficiency over prior MAC-tree and fixed-shape SA designs.

References

- [1] Amey Agrawal, Ashish Panwar, Jayashree Mohan, Nipun Kwatra, Bhargav S Gulavani, and Ramachandran Ramjee. 2023. Sarathi: Efficient llm inference by piggybacking decodes with chunked prefills. *arXiv preprint arXiv:2308.16369* (2023).
- [2] Jonathan Chang, Yen-Huei Chen, Wei-Min Chan, Sahil Preet Singh, Hank Cheng, Hidehiro Fujiwara, Jih-Yu Lin, Kao-Cheng Lin, John Hung, Robin Lee, et al. 2017. 12.1 a 7nm 256mb sram in high-k metal-gate finfet technology with write-assist circuitry for low-v min applications. In *2017 IEEE International Solid-State Circuits Conference (ISSCC)*. IEEE, Piscataway, NJ, USA, 206–207.
- [3] Rongmei Chen, Pieter Weckx, Shairfe Muhammad Salahuddin, S-W Kim, Giuliano Sisto, Geert Van Der Plas, Michele Stucchi, Rogier Baert, Peter Debacker, MH Na, et al. 2020. 3D-optimized SRAM macro design and application to memory-on-logic 3D-IC at advanced nodes. In *2020 IEEE International Electron Devices Meeting (IEDM)*. IEEE, IEEE, Piscataway, NJ, USA, 15–2.
- [4] Yu-Hsin Chen, Tushar Krishna, Joel S Emer, and Vivienne Sze. 2016. Eyeriss: An energy-efficient reconfigurable accelerator for deep convolutional neural networks. *IEEE journal of solid-state circuits* 52, 1 (2016), 127–138.

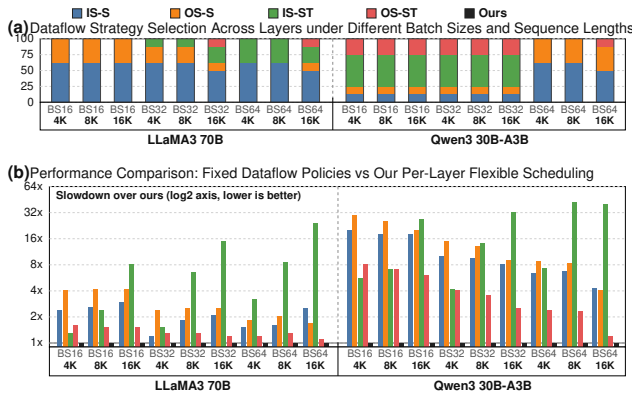


Figure 13: Per-Layer Scheduling Strategy Mix and Fixed-Scheduling Slowdown

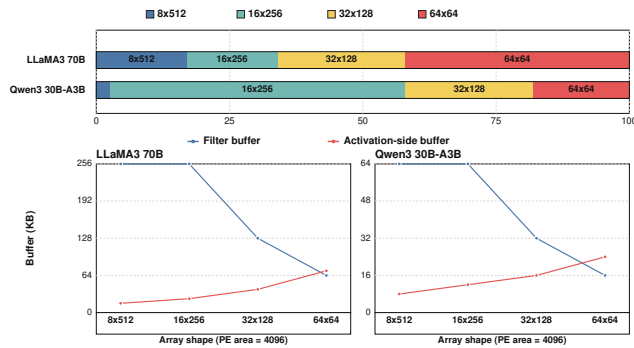


Figure 14: Array Demand and Buffer Trade-offs

[5] Jack Choquette. 2023. NVIDIA Hopper H100 GPU: Scaling Performance. *IEEE Micro* 43, 3 (2023), 9–17.

[6] Lawrence T Clark, Vinay Vashishtha, Lucian Shifren, Aditya Gujja, Saurabh Sinha, Brian Cline, Chandrasekaran Ramamurthy, and Greg Yeric. 2016. ASAP7: A 7-nm finFET predictive process design kit. *Microelectronics Journal* 53 (2016), 105–115.

[7] DeepSeek-AI. 2024. DeepSeek-V3 Technical Report. arXiv preprint arXiv:2412.19437. arXiv:2412.19437

[8] Mingyu Gao, Jing Pu, Xuan Yang, Mark Horowitz, and Christos Kozyrakis. 2017. Tetris: Scalable and efficient neural network acceleration with 3d memory. In *Proceedings of the Twenty-Second International Conference on Architectural Support for Programming Languages and Operating Systems*. ACM, New York, NY, USA, 751–764.

[9] Hasan Genc, Seah Kim, Alon Amid, Ameer Haj-Ali, Vighnesh Iyer, Pranav Prakash, Jerry Zhao, Daniel Grubb, Harrison Liew, Howard Mao, et al. 2021. Gemmini: Enabling systematic deep-learning architecture evaluation via full-stack integration. In *2021 58th ACM/IEEE Design Automation Conference (DAC)*. IEEE, ACM, New York, NY, USA, 769–774.

[10] Sorush Ghodrati, Byung Hoon Ahn, Joon Kyung Kim, Sean Kinzer, Brahendra Reddy Yatham, Navateja Alla, Hardik Sharma, Mohammad Alian, Eiman Ebrahimi, Nam Sung Kim, et al. 2020. Planaria: Dynamic architecture fission for spatial multi-tenant acceleration of deep neural networks. In *2020 53rd Annual IEEE/ACM International Symposium on Microarchitecture (MICRO)*. IEEE, 681–697.

[11] Aaron Grattafiori et al. 2024. The Llama 3 Herd of Models. arXiv preprint arXiv:2407.21783. arXiv:2407.21783

[12] Cong Guo, Yangjie Zhou, Jingwen Leng, Yuhao Zhu, Zidong Du, Quan Chen, Chao Li, Bin Yao, and Minyi Guo. 2020. Balancing Efficiency and Flexibility for DNN Acceleration via Temporal GPU-Systolic Array Integration. In *2020 57th ACM/IEEE Design Automation Conference (DAC)*. ACM, New York, NY, USA, 1–6. <https://doi.org/10.1109/DAC18072.2020.9218732> doi: 10.1109/DAC18072.2020.9218732.

[13] Meng Han, Liang Wang, Limin Xiao, et al. 2024. ReDas: A Lightweight Architecture for Supporting Fine-Grained Reshaping and Multiple Dataflows on Systolic Array. *IEEE Trans. Comput.* 73, 10 (2024), 2501–2515.

[14] Sanghyeok Han, Byungkuk Yoon, Gyeonghwan Park, Choungki Song, Dongkyun Kim, and Jae-Joon Kim. 2025. Near-Memory LLM Inference Processor based on 3D DRAM-to-logic Hybrid Bonding. In *2025 62nd ACM/IEEE Design Automation Conference (DAC)*. IEEE, ACM, New York, NY, USA, 1–7.

[15] Siyuan He, Peiran Yan, Yandong He, Youwei Zhuo, and Tianyu Jia. 2025. Tasa: Thermal-aware 3D-Stacked Architecture Design with Bandwidth Sharing for LLM Inference. In *2025 IEEE/ACM International Conference on Computer Aided Design (ICCAD)*. IEEE, IEEE, Piscataway, NJ, USA, 1–9.

[16] Guseul Heo, Sangyeop Lee, Jaehong Cho, Hyunmin Choi, Sanghyeon Lee, Hyungkyu Ham, Gwangsun Kim, Divya Mahajan, and Jongse Park. 2024. Npu-pim heterogeneous acceleration for batched llm inference. In *Proceedings of the 29th ACM International Conference on Architectural Support for Programming Languages and Operating Systems, Volume 3*. ACM, New York, NY, USA, 722–737.

[17] Haochen Huang, Shuzhang Zhong, Zhe Zhang, Shuangchen Li, Dimin Niu, Hongzhong Zheng, Runsheng Wang, and Meng Li. 2025. HD-MoE: Hybrid and Dynamic Parallelism for Mixture-of-Expert LLMs with 3D Near-Memory Processing. In *2025 IEEE/ACM International Conference on Computer Aided Design (ICCAD)*. IEEE, IEEE, Piscataway, NJ, USA, 1–9.

[18] Albert Q. Jiang et al. 2024. Mixtral of Experts. arXiv preprint arXiv:2401.04088. arXiv:2401.04088

[19] Norman Jouppi and Sridhar Lakshmanamurthy. 2025. Ironwood: Delivering best in class perf, perf/TCO and perf/Watt for reasoning model training and serving. Presentation at Hot Chips 2025. Hot Chips 37.

[20] Yuhao Ju and Jie Gu. 2022. A 65nm systolic neural CPU processor for combined deep learning and general-purpose computing with 95% PE utilization, high data locality and enhanced end-to-end performance. In *2022 IEEE International Solid-State Circuits Conference (ISSCC)*, Vol. 65. IEEE, IEEE, Piscataway, NJ, USA, 1–3. doi: 10.1109/ISSCC42614.2022.9731757.

[21] Kwiwook Kim and Myeong-jae Park. 2024. Present and future, challenges of high bandwidth memory (HBM). In *2024 IEEE International Memory Workshop (IMW)*. IEEE, 1–4.

[22] Yoongu Kim, Weikun Yang, and Onur Mutlu. 2015. Ramulator: A Fast and Extensible DRAM Simulator. *IEEE Computer Architecture Letters* 15, 1 (2015), 45–48. <https://doi.org/10.1109/LCA.2015.2414456>

[23] John H Lau. 2022. Recent advances and trends in advanced packaging. *IEEE Transactions on Components, Packaging and Manufacturing Technology* 12, 2 (2022), 228–252.

[24] Jounghoo Lee, Jinwoo Choi, Jaeyeon Kim, Jinho Lee, and Youngsok Kim. 2021. Dataflow mirroring: Architectural support for highly efficient fine-grained spatial multitasking on systolic-array npus. In *2021 58th ACM/IEEE Design Automation Conference (DAC)*. ACM, ACM, New York, NY, USA, 247–252. doi: 10.1109/DAC18074.2021.9586312.

[25] Seongju Lee, Kyuyoung Kim, Sanghoon Oh, Joonhong Park, Gimoon Hong, Dongyoun Ka, Kyudong Hwang, Jeongje Park, Kyeongpil Kang, Jungyeon Kim, et al. 2022. A 1ynn 1.25 V 8Gb, 16Gb/s/pin GDDR6-based accelerator-in-memory supporting 1TFLOPS MAC operation and various activation functions for deep-learning applications. In *2022 IEEE International Solid-State Circuits Conference (ISSCC)*, Vol. 65. IEEE, 1–3.

[26] Baolin Li, Yankai Jiang, Vijay Gadepally, and Devesh Tiwari. 2024. Llm inference serving: Survey of recent advances and opportunities. In *2024 IEEE High Performance Extreme Computing Conference (HPEC)*. IEEE, 1–8.

[27] Cong Li, Yihan Yin, Xintong Wu, Jingchen Zhu, Zhutian Gao, Dimin Niu, Qiang Wu, Xin Si, Yuan Xie, Chen Zhang, et al. 2025. H2-llm: Hardware-dataflow co-exploration for heterogeneous hybrid-bonding-based low-batch llm inference. In *Proceedings of the 52nd Annual International Symposium on Computer Architecture*. ACM, New York, NY, USA, 194–210.

[28] Cong Li, Yihan Yin, Chenhao Xue, et al. 2026. Hardware-Software Co-design for 3D-DRAM-based LLM Serving Accelerator. arXiv preprint arXiv:2603.04797. arXiv:2603.04797

[29] Mateo Vázquez Maceiras, Muhammad Waqar Azhar, and Pedro Trancoso. 2022. VSA: A Hybrid Vector-Systolic Architecture. In *2022 IEEE 40th International Conference on Computer Design (ICCD)*. IEEE, Piscataway, NJ, USA, 368–376. <https://doi.org/10.1109/ICCD56317.2022.00061> doi: 10.1109/ICCD56317.2022.00061.

[30] Ki-Il Moon, Ho-Young Son, and Kangwook Lee. 2023. Advanced packaging technologies in memory applications for future generative AI era. In *2023 International Electron Devices Meeting (IEDM)*. IEEE, 1–4.

[31] Yue Pan, Zihan Xia, Po-Kai Hsu, Lanxiang Hu, Hyungyo Kim, Janak Sharda, Minxuan Zhou, Nam Sung Kim, Shimeng Yu, Tajana Rosing, et al. 2025. Stratum: System-Hardware Co-Design with Tiered Monolithic 3D-Stackable DRAM for Efficient MoE Serving. In *Proceedings of the 58th IEEE/ACM International Symposium on Microarchitecture*. ACM, New York, NY, USA, 1–17.

[32] Jaehyun Park, Jaewan Choi, Kwanhee Kyung, Michael Jaemin Kim, Yongsuk Kwon, Nam Sung Kim, and Jung Ho Ahn. 2024. Attac! unleashing the power of

- pim for batched transformer-based generative model inference. In *Proceedings of the 29th ACM International Conference on Architectural Support for Programming Languages and Operating Systems, Volume 2*. ACM, New York, NY, USA, 103–119.
- [33] Qwen Team. 2025. Qwen3 Technical Report. arXiv preprint arXiv:2505.09388. arXiv:2505.09388
- [34] Ritik Raj et al. 2025. SCALE-Sim v3: A Modular Cycle-Accurate Systolic Accelerator Simulator for End-to-End System Analysis. arXiv preprint arXiv:2504.15377. arXiv:2504.15377
- [35] Ananda Samajdar, Eric Qin, Michael Pellauer, and Tushar Krishna. 2022. Self adaptive reconfigurable arrays (SARA) learning flexible GEMM accelerator configuration and mapping-space using ML. In *Proceedings of the 59th ACM/IEEE Design Automation Conference (DAC)*. ACM, New York, NY, USA, 583–588. <https://doi.org/10.1145/3489517.3530506>
- [36] Alireza Shafaei, Yanzhi Wang, Xue Lin, and Massoud Pedram. 2014. FinCACTI: Architectural analysis and modeling of caches with deeply-scaled FinFET devices. In *2014 IEEE Computer Society Annual Symposium on VLSI*. IEEE, ACM, New York, NY, USA, 290–295.
- [37] Stefaan Van Huylenbroeck, Michele Stucchi, Yunlong Li, John Slabbekoorn, Nina Tutunjan, Stefano Sardo, Nicolas Jourdan, Lieve Bogaerts, Filip Beirnaert, Gerald Beyer, et al. 2016. Small pitch, high aspect ratio via-last TSV module. In *2016 IEEE 66th Electronic Components and Technology Conference (ECTC)*. IEEE, IEEE, Piscataway, NJ, USA, 43–49.
- [38] Haoran Wu et al. 2025. Combating the memory walls: Optimization pathways for long-context agentic llm inference. arXiv preprint arXiv:2509.09505. arXiv:2509.09505
- [39] Sungmin Yun, Kwanhee Kyung, Juhwan Cho, Jaewan Choi, Jongmin Kim, Byeongho Kim, Sukhan Lee, Kyomin Sohn, and Jung Ho Ahn. 2024. Duplex: A device for large language models with mixture of experts, grouped query attention, and continuous batching. In *2024 57th IEEE/ACM International Symposium on Microarchitecture (MICRO)*. IEEE, IEEE, Piscataway, NJ, USA, 1429–1443.
- [40] Susan Zhang, Stephen Roller, Naman Goyal, Mikel Artetxe, Moya Chen, Shuo-hui Chen, Christopher Dewan, Mona Diab, Xian Li, Xi Victoria Lin, Todor Mihaylov, Myle Ott, Sam Shleifer, Kurt Shuster, Daniel Simig, Punit Singh Koura, Anjali Sridhar, Tianlu Wang, and Luke Zettlemoyer. 2022. OPT: Open Pre-trained Transformer Language Models. arXiv preprint arXiv:2205.01068. arXiv:2205.01068 [cs.CL]
- [41] Zixuan Zhou, Xuefei Ning, Ke Hong, Tianyu Fu, Jiaming Xu, Shiyao Li, Yuming Lou, Luning Wang, Zhihang Yuan, Xiuhong Li, et al. 2024. A survey on efficient inference for large language models. *arXiv preprint arXiv:2404.14294* (2024).